


 Cite this: *Nanoscale*, 2021, **13**, 3027

## Electron cloud migration effect-induced lithiophobicity/lithiophilicity transformation for dendrite-free lithium metal anodes†

 Wenyuan Zou,<sup>‡a</sup> Qianyao Li,<sup>‡a</sup> Zhe Zhu,<sup>a</sup> Lulu Du,<sup>a</sup> Xinyin Cai,<sup>a</sup> Yiming Chen,<sup>a</sup> Gang Zhang,<sup>a</sup> Song Hu,<sup>a</sup> Feilong Gong,<sup>id c</sup> Lin Xu<sup>id \*a,b</sup> and Liqiang Mai<sup>id a,b</sup>

Enabling stable lithium metal anodes is significant for developing electrochemical energy storage systems with higher energy density. However, safety hazards, infinite volume expansion, and low coulombic efficiency (CE) of lithium metal anodes always hinder their practical application. Herein, a nano-thickness lithiophilic Cu–Ni bimetallic coating was synthesized to prepare dendrite-free lithium metal anodes. The electron cloud migration effect caused by the different electronegativities of Cu and Ni can achieve lithiophobicity/lithiophilicity transformation and thus promote uniform Li deposition/dissolution. By changing the ratio of Cu to Ni, the electron cloud migration can be reasonably adjusted for obtaining dendrite-free lithium anodes. As a result, the as-obtained Cu–Ni bimetallic coating is able to guarantee dendrite-free lithium metal anodes with a stable long cycling time (>1500 hours) and a small voltage hysteresis (~26 mV). In addition, full cells with LiFePO<sub>4</sub> as a cathode present excellent cycling stability and high coulombic efficiency. This work can open a new avenue for optimizing the lithiophilicity of materials and realizing dendrite-free anodes.

Received 23rd November 2020,

Accepted 18th January 2021

DOI: 10.1039/d0nr08343g

[rsc.li/nanoscale](http://rsc.li/nanoscale)

### Introduction

The commercialization of lithium-ion batteries (LIBs) has been developing for nearly 30 years. The widespread application of LIBs has been changing the lifestyle of the modern society.<sup>1,2</sup> However, commercial LIBs using graphite anodes (372 mA h g<sup>-1</sup>) have difficulty in meeting the increasing energy density demand due to the low specific capacity of graphite.<sup>3,4</sup> Therefore, the exploitation of high specific capacity anodes is an important part in the research of new generation energy storage systems. According to the reported research results, the lithium metal has a higher theoretical capacity (3860 mA h g<sup>-1</sup>) and the lowest electrochemical reduction potential (–3.04 V vs. the standard hydrogen electrode).<sup>5</sup> However, there still exist many problems that severely limit the large-scale application of lithium metal anodes: (1) Lithium dendrites: in the

cycling of charge and discharge, the fast-growing lithium dendrites can easily pierce the separator, which will lead to short circuits and even violent explosions.<sup>6,7</sup> (2) Infinite volume expansion: continuous volume change derived from the “hostless” nature of lithium metal anodes will bring about great challenges to the solid electrolyte interphase (SEI) stability.<sup>8,9</sup> (3) Low coulombic efficiency: a serious irreversible reaction and excessive “dead lithium” will lead to a decrease of coulombic efficiency (CE).<sup>10–13</sup>

In order to solve the above problems, current research on lithium metal anodes mainly focuses on the following aspects: one is to optimize the electrolyte composition (such as introducing additives, changing the electrolyte composition, *etc.*), which can restrain the decomposition of the electrolyte and the generation of “dead lithium” by forming a stable and dense SEI.<sup>14,15</sup> Another way is to construct a layer of stable artificial SEI, such as the TiO<sub>2</sub>/lithium *n*-butoxide hybrid artificial SEI, Li<sub>4</sub>SiO<sub>4</sub>-based hybrid artificial SEI and so on, in advance to protect lithium metal anodes.<sup>16,17</sup> The rapid growth of lithium dendrites can be significantly suppressed by promoting uniform deposition of Li.<sup>18–20</sup> Besides, the utilization of solid electrolyte is also a powerful strategy, which can avoid the irreversible reaction and safety problems caused by lithium dendrites at the same time.<sup>21–23</sup> However, problems such as high production cost, complex preparation process, and poor interface stability still hinder the further development of these methods.<sup>24–28</sup> In addition to these methods,

<sup>a</sup>State Key Laboratory of Advanced Technology for Materials Synthesis and Processing, School of Materials Science and Engineering, Wuhan University of Technology, Luoshi Road 122, Wuhan, 430070, P. R. China.  
E-mail: [linxu@whut.edu.cn](mailto:linxu@whut.edu.cn)

<sup>b</sup>Foshan Xianhu Laboratory of the Advanced Energy Science and Technology Guangdong Laboratory, Foshan 528200, China

<sup>c</sup>Key Laboratory of Surface and Interface Science and Technology, Zhengzhou University of Light Industry, Zhengzhou, 450002, Henan, P. R. China

†Electronic supplementary information (ESI) available. See DOI: 10.1039/d0nr08343g

‡These authors contributed equally to this work.

constructing a 3D host is also a promising strategy to modify lithium metal anodes, which is able to ease the rapid growth of lithium dendrites and suppress the violent volume change.<sup>29–31</sup> Nevertheless, a 3D host (such as nickel foam (NF), copper foam (CF), carbon paper, *etc.*) is unable to fundamentally prevent the growth of lithium dendrites due to intrinsic lithiophobicity. A LiF-rich host was rationally constructed to achieve dendrite-free lithium metal anodes.<sup>32</sup>

Herein, we propose a strategy achieving the lithiophobicity/lithiophilicity transformation of NF *via* introducing a nanometer-thick Cu–Ni bimetallic coating (Cu–Ni) to prepare dendrite-free lithium metal anodes. Compared to NF and CF, Cu–Ni shows superior lithiophilicity and better electrochemical performance. There is an electron cloud migration in the bimetallic coating due to the different electronegativities between Cu and Ni. We adjust the electron cloud migration by changing the ratio of Cu to Ni to realize reasonable distribution of surface charge density, which contributes to a stronger adsorption energy of Li. Consequently, symmetric cells assembled with Li@Cu–Ni exhibit a longer cycling life (>1500 hours) and a smaller voltage hysteresis (26 mV) at 1 mA cm<sup>-2</sup>. Furthermore, full cells assembled with a LiFePO<sub>4</sub> (LFP) cathode and a Li@Cu–Ni composite anode show perfect cycling stability and excellent coulombic efficiency.

## Experimental section

All the chemical reagents were directly used without additional purification.

### Preparation of a nickel foam sheet, copper foam sheet, and Cu–Ni bimetallic coating

Nickel foam (NF) and copper foam (CF) were cut into 2 × 2 cm<sup>2</sup> using a paper cutter machine. In a typical procedure, NF sheets and CF sheets were ultrasonically washed in dilute hydrochloric acid, acetone, and deionized water for 30 minutes, respectively. The cleaned NF sheets and CF sheets finally were dried for 5 hours in a vacuum oven. A Cu–Ni bimetallic coating (Cu–Ni) was synthesized by an electroplating method. The electroplating solution consisted of 13.1425 g of nickel sulfate hexahydrate, 0.399025 g of anhydrous cupric sulfate, 1.545 g of boric acid and 50 mL of H<sub>2</sub>O. The electroplating process was performed at room temperature in a three-electrode system with a counter electrode (Pt) and a reference electrode (calomel). A 2 × 2 cm<sup>2</sup> NF sheet was used as the working electrode. The electroplating constant voltage was set to 0.75 V and the electroplating time was fixed at 400 s. NF sheets loaded with the Cu–Ni bimetallic coating were washed in turn with ethanol and H<sub>2</sub>O to remove the residual electroplating solution and dried in a vacuum oven for 3 hours.

### Preparation of Li@Cu–Ni, Li@NF, and Li@CF composite anodes

Cu–Ni sheets, NF sheets, and CF sheets were cut into regular disks with a diameter of 1.4 cm, respectively. Lithium sheets

were used as the anode and Cu–Ni disks, NF disks, and CF disks were used as the cathode. CR2016 coin cells were assembled to electrodeposit Li to prepare composite metal lithium anodes (these electrodes were denoted as Li@Cu–Ni, Li@NF, and Li@CF). 3 mA h cm<sup>-2</sup> lithium was electrodeposited to form Li@Cu–Ni, Li@NF, and Li@CF composite anodes at a current density of 0.5 mA cm<sup>-2</sup>.

### Materials characterization

The morphological features of Cu–Ni and other materials were characterized using a scanning electron microscope (SEM, JEOL JSM-7100F). An Oxford IE250 system was used to record energy dispersive X-ray spectra (EDS). A JEM-2100F/Titan G260-300 transmission electron microscope was used to obtain high-resolution TEM (HRTEM) images and selected-area electron diffraction (SAED) patterns. X-ray diffraction (XRD) patterns were obtained using a D8 Discover X-ray diffractometer (Cu K $\alpha$  radiation,  $\lambda = 1.054056 \text{ \AA}$ ). An ESCALAB 250Xi was used to record X-ray photoelectron spectra (XPS). Grazing incidence X-ray diffraction (GIXRD) patterns were obtained with a powder X-ray diffractometer (XRD; PANalytical, Empyrean), using Cu K $\alpha$  with  $2\theta$  in the range of 10°–80°.

## Results and discussion

Cu<sup>2+</sup> and Ni<sup>2+</sup> were co-deposited on NF using the electroplating method at a constant voltage to form lithiophilic Cu–Ni (Fig. 1a). Then the composite lithium anode was synthesized by an electrodeposition method. In order to obtain the optimal conditions, it is significant to determine an ideal electroplating time and voltage. As shown in Fig. S1a and b,† the X-ray diffraction (XRD) patterns of these samples from 150 s to 200 s show only three peaks (44.57°, 51.94°, and 76.46°), which belong to the peaks of metal Ni. When the electroplating time is increased to 250 s, the peak of Cu–Ni (43.74°) appears (because the XRD peak intensity of Ni is relatively strong, the other peaks are weak.) and its intensity increases with time. The shift of the peak position is mainly caused by different deposition rates of Cu<sup>2+</sup> and Ni<sup>2+</sup>.<sup>33</sup> At the same time, the detailed morphological information of these samples was also obtained using scanning electron microscopy (SEM). CF and NF show a similar three-dimensional structure (Fig. S2a and b, ESI†). It is obvious that there are only scattered Cu–Ni bimetallic particles on the substrate surface when the electroplating time is less than 300 s (Fig. S2c and d, ESI†). After the electroplating time is increased to 400 s, the NF surface is covered with a dense and uniform Cu–Ni (Fig. S2e, ESI†). However, when the electroplating time is extended to 500 s, abnormal spike-like particles begin to appear, which is bad for the plating/stripping of Li (Fig. S2f, ESI†). As a result, 400 s is a reasonable electroplating time. Otherwise, the BET specific surface areas of Cu–Ni, CF, and NF were found to be 1.6404 m<sup>2</sup> g<sup>-1</sup>, 1.0947 m<sup>2</sup> g<sup>-1</sup> and 1.5616 m<sup>2</sup> g<sup>-1</sup>, indicating that the surface structure does not obviously affect the specific surface area (Fig. S3, ESI†). On the other hand, it is necessary to find a

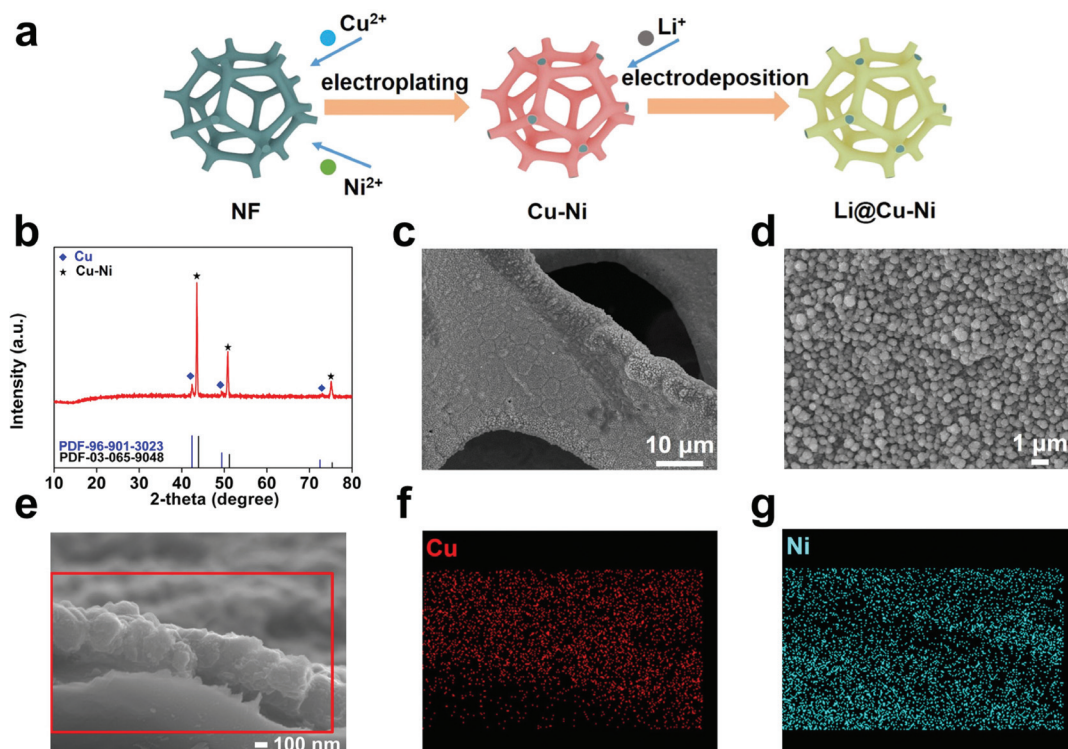


**Fig. 1** Synthesis process and morphological characterization: (a) Schematic illustration of the synthesis process of Li@Cu-Ni, (b) GIXRD of Cu-Ni, (c and d) SEM images of Cu-Ni, (e) cross-sectional SEM image of Cu-Ni, and (f and g) EDS mapping results of Cu-Ni.

rational electroplating voltage to control the ratio of Cu to Ni.<sup>33</sup> The relative contents of Cu and Ni decrease and increase, respectively, with the increase of voltage. It can be seen from Fig. S4† that the Cu-Ni bimetallic coatings synthesized at different electroplating voltages have consistent morphologies, which can further exclude the influence of surface structure on Li plating/stripping behavior. It can be seen from Fig. S5† that during the initial phase of Li deposition, there is an obvious voltage drop, and then a gradually stable voltage platform appears. Therefore, lithium nucleation overpotential is defined by the difference between the voltage platform and the voltage drop.<sup>34</sup> It can be clearly seen that Cu-Ni obtained at 0.75 V has the smallest Li nucleation overpotential, which facilitates the uniform deposition of Li. This phenomenon indicates that Cu-Ni-0.75 V has the optimal lithiophilicity (nucleation overpotential is only 18 mV), which may be caused by the electron cloud migration effect (this phenomenon will be discussed later). In addition, the XRD pattern of different electroplating voltages shows the peaks of Cu-Ni and Ni (Fig. S6, ESI†). Eventually, we decided to select 400 s and 0.75 V as the ideal electroplating time and voltage (the Cu-Ni samples mentioned later are all obtained at 400 s and 0.75 V), respectively.

The composition and structural properties of Cu-Ni were further characterized and analysed. The grazing incidence X-ray diffraction (GIXRD) pattern utilized to characterize the composition of Cu-Ni shows three diffraction peaks (43.93°, 51.07°, and 75.22°) corresponding to the Cu-Ni bimetal. The other peaks belong to the metal Cu which is caused by the

remaining metal Cu during the electroplating process (Fig. 1b). Meanwhile, the SEM images show that Cu-Ni consists of particles with uniform size, which grow densely and are uniformly distributed (Fig. 1c and d). The energy dispersive spectroscopy (EDS) mapping images exhibit the uniform distribution of Cu and Ni, suggesting the bimetallic structure (Fig. S7a-f, ESI†). The cross-sectional SEM images of Cu-Ni show that the thickness of the coating is about 400 nm and the EDS mapping images further confirm that the elements (Cu and Ni) are evenly distributed in the vertical direction, which is consistent with the typical observation in GIXRD (Fig. 1e-g). The detailed chemical and structural information of Cu and Ni in the bimetallic coating was further explored by X-ray photoelectron spectroscopy (XPS). CF and NF were selected as the sources of Cu and Ni. As seen in Fig. 2a, the Cu 2p spectrum of Cu-Ni shows a pair of 2p<sub>1/2</sub> and 2p<sub>3/2</sub> peaks (932.08 eV and 951.92 eV), which may correspond to Cu<sup>0</sup> or Cu<sub>2</sub>O. By further fitting the O 1s spectrum of Cu-Ni, the presence of Cu<sub>2</sub>O can be clearly observed (Fig. S8a, ESI†).<sup>35</sup> The other two peaks (934.59 eV and 954.36 eV) and their satellite peaks are caused by Cu<sup>2+</sup>, which is due to the fact that Cu is easily oxidized in the air.<sup>36</sup> The O 1s spectrum of CF is similar to that of Cu-Ni (Fig. S8b, ESI†). On the other hand, there are some peaks located at 856.2 eV, 873.89 eV, 861.76 eV, and 879.57 eV in the Ni 2p spectrum of Cu-Ni (Fig. 2b). The binding energies of 856.2 eV and 873.89 eV can be attributed to Ni<sup>2+</sup>, which is mainly caused by the easy oxidation of metallic Ni in the air.<sup>36</sup> The remaining peaks are the satellite peaks

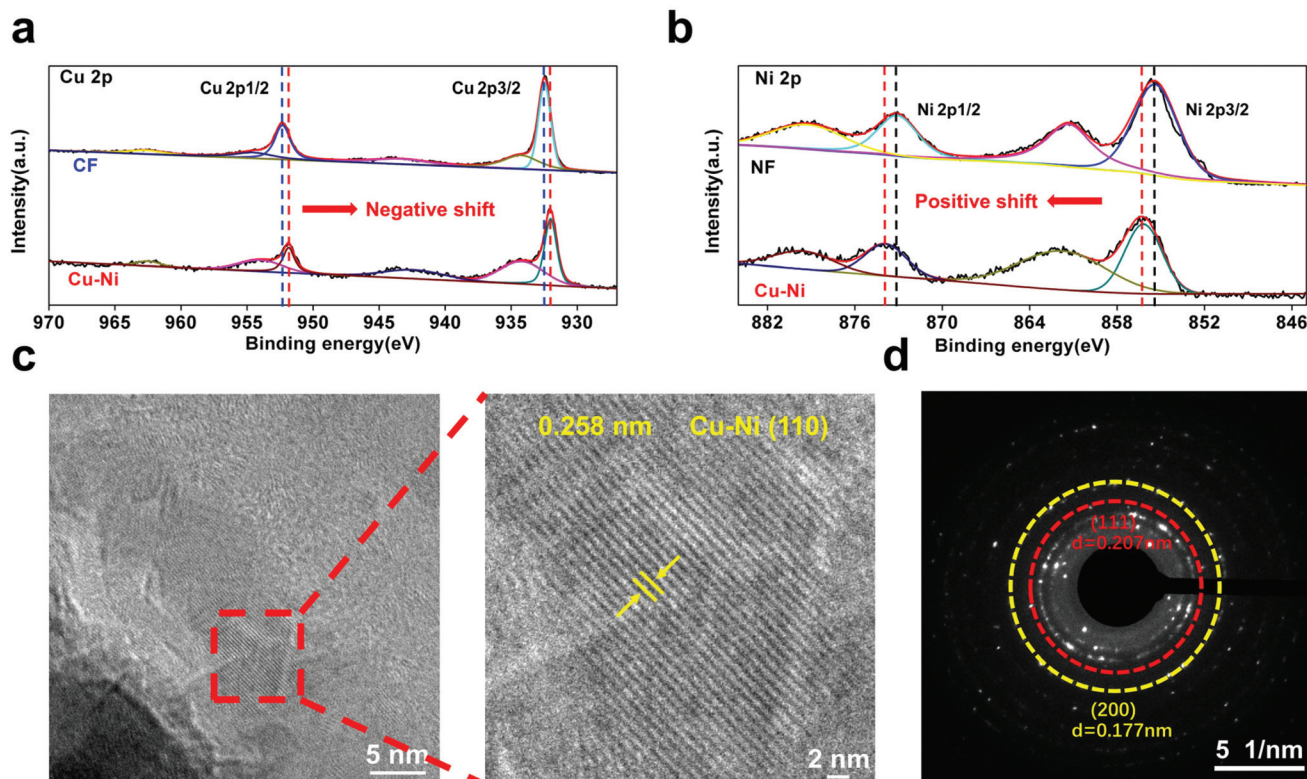
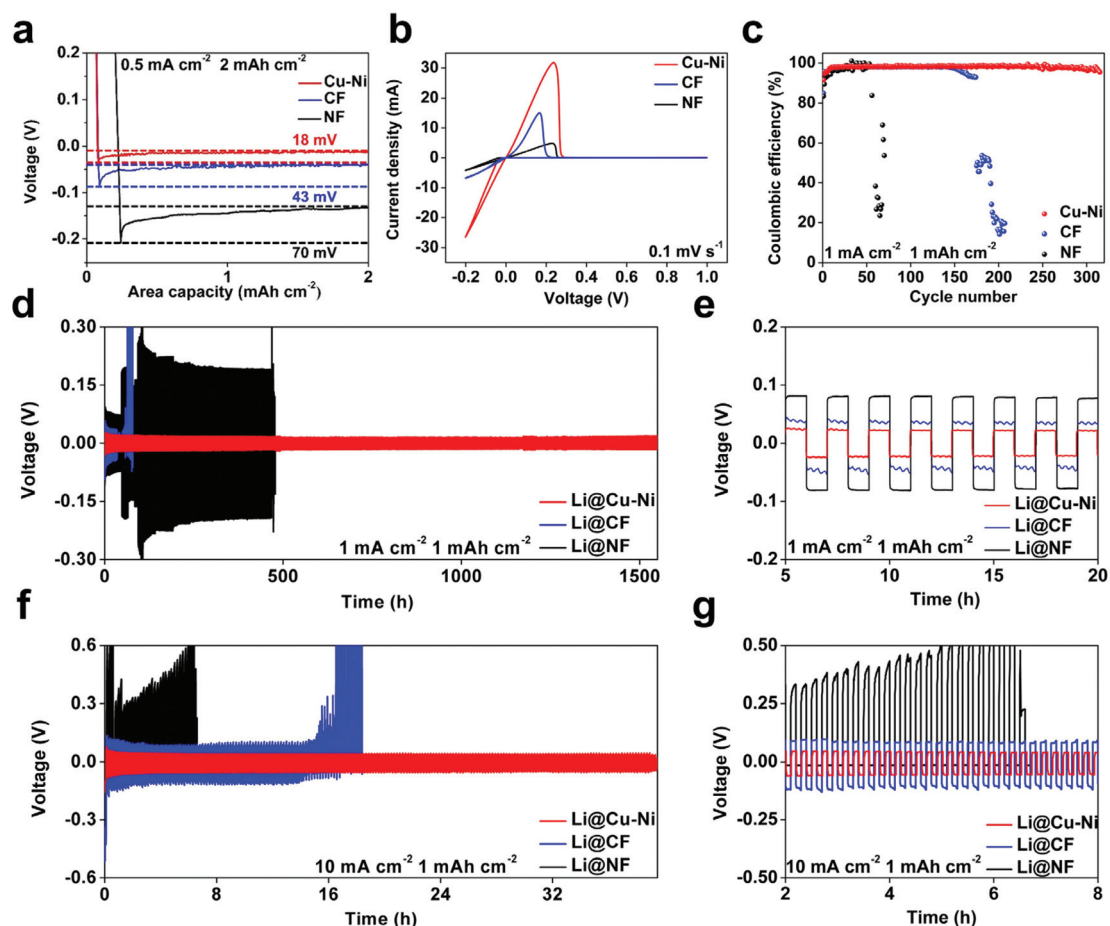


Fig. 2 Structural characterization of Cu–Ni: (a) Cu 2p XPS spectra of Cu–Ni and CF, (b) Ni 2p XPS spectra of Cu–Ni and NF, (c) HRTEM images of Cu–Ni, and (d) SAED pattern of Cu–Ni.

of  $\text{Ni}^{2+}$ . The lack of  $\text{Ni}^0$  peaks is mainly due to the detection depth of XPS. Furthermore, by comparing the positions of the Cu 2p peaks and the Ni 2p peaks in the XPS spectra of Cu–Ni with respect to CF and NF, it can be found that the Cu 2p peak of Cu–Ni shows a negative shift to a lower binding energy while the binding energy change of the Ni 2p peak is in the opposite direction, which can be ascribed to the charge transfer from the less electronegative Ni to the more electronegative Cu.<sup>37–39</sup> The XPS spectra of Cu–Ni synthesized at different electroplating voltages (0.7 V, 0.8 V and 0.75 V), CF and NF are shown in Fig. S9a–d.† In order to determine the relationship between electron cloud migration and the atomic ratio of Cu to Ni, the atomic ratios of Cu to Ni of these samples were determined by XPS semi-quantitative analysis. It can be clearly seen that Cu–Ni-0.75 V is composed of a 1 : 1 ratio of Cu to Ni. The ratio of Cu–Ni-0.7 V and Cu–Ni-0.8 V is about 1.5 : 1 and 0.5 : 1, respectively (Table S1, ESI†). Notably, the Ni 2p peaks of all Cu–Ni samples are positively shifted, and the degree of shift increases with the decrease of the relative content of Ni, indicating that more electron clouds migrate from Ni to Cu as the relative content of Ni decreases (Fig. S10, ESI†).<sup>39–42</sup> As seen in Fig. S5,† Cu–Ni obtained at 0.75 V (Cu : Ni = 1 : 1) has the optimal lithophilicity (nucleation overpotential is only 18 mV), which indicates that electron cloud migration in Cu–Ni obtained at 0.75 V can effectively induce lithiophobicity/lithophilicity transformation. Therefore, by changing the ratio

of Cu to Ni, the electron cloud migration can be adjusted for improving the lithophilicity of the material. Furthermore, high-resolution transmission electron microscopy (HRTEM) was used to observe the microstructure of Cu–Ni. Cu–Ni shows a characteristic lattice fringe of 0.258 nm for the (110) crystal planes of Cu–Ni (Fig. 2c). Fig. 2d shows the selected area electron diffraction (SAED) pattern, and the electron diffraction spot can be ascribed to the (111) and (200) planes of Cu–Ni, suggesting the high crystallinity of Cu–Ni.

Galvanostatic Li deposition was performed to explore the Li deposition behaviors. Fig. 3a shows the nucleation overpotential of Cu–Ni, NF and CF with the same discharge current density ( $0.5 \text{ mA cm}^{-2}$ ) and deposition capacity ( $2 \text{ mA h cm}^{-2}$ ). The initial Li deposition on Cu–Ni shows a smaller voltage drop, and the final nucleation overpotential is only 18 mV. In comparison, it can be clearly seen that the nucleation overpotentials of NF and CF are 70 mV and 43 mV, respectively, reflecting their lithiophobicity, which will aggravate the growth of lithium dendrites. The significant reduction of the nucleation overpotential indicates that Cu–Ni has been transformed from lithiophobicity to lithophilicity by the electron cloud migration effect. It can be seen from the cyclic voltammetry curve that whether it is NF, CF, or Cu–Ni, only the redox peaks of Li deposition and dissolution appear (Fig. 3b).<sup>43</sup> This implies that Cu–Ni will not react with Li to form an alloy. The alloying reaction will result in a rapid increase in the volume



**Fig. 3** Electrochemical performance of Cu-Ni. (a) Nucleation overpotential of galvanostatic Li deposition on Cu-Ni, NF, and CF substrates at a current density of  $0.5 \text{ mA cm}^{-2}$ . (b) Cyclic voltammetry curve of Li deposition/dissolution on Cu-Ni, NF and CF. (c) The CE of Li deposition on Cu-Ni, NF and CF at a current density of  $1 \text{ mA cm}^{-2}$  with a Li capacity of  $1 \text{ mA h cm}^{-2}$ . (d) Galvanostatic charge-discharge curves of symmetrical cells assembled with Li@Cu-Ni, Li@NF and Li@CF electrodes at a current density of  $1 \text{ mA cm}^{-2}$  with a cycling capacity of  $1 \text{ mA h cm}^{-2}$ . (e) Magnified charge-discharge curves for 5–20 hours. (f) Galvanostatic charge-discharge curves of symmetrical cells assembled with Li@Cu-Ni, Li@NF and Li@CF electrodes at a current density of  $10 \text{ mA cm}^{-2}$  with a cycling capacity of  $1 \text{ mA h cm}^{-2}$ . (g) Magnified charge-discharge curves for 2–8 hours.

of the anode ( $\sim 400\%$  for Si), forming a huge obstacle to its commercialization.<sup>44</sup> Moreover, the CE of Cu-Ni, NF and CF can accurately reflect the lithium deposition/dissolution efficiency on different substrates. As illustrated in Fig. 3c, Cu-Ni can reach a high CE (99.46%) at  $1 \text{ mA cm}^{-2}$ . Even after 310 cycles, the CE still remains at 98.1%. In comparison, the CE of NF and CF present fast decay and huge fluctuations under the same conditions. Furthermore, the average coulombic efficiency of Li@Cu-Ni|Cu-Ni, Li@CF|CF and Li@NF|NF was evaluated, respectively (Fig. S11a–c, ESI†). Compared with Li@CF|CF and Li@NF|NF, the average coulombic efficiency of Li@Cu-Ni|Cu-Ni has been significantly improved, indicating that the lithiophilicity of Cu-Ni regulates the electrochemical behavior of Li deposition and dissolution. This suggests that the generation of “dead lithium” is suppressed (this conclusion will be verified later.), and better reversibility is achieved due to the lithiophobicity/lithiophilicity transformation induced by the electron cloud migration effect. In addition, cycling stability is another important indicator,

including the cycling time and voltage hysteresis. The definition of voltage hysteresis is considered to be the sum of Li deposition and Li dissolution overpotential. Symmetrical cells were used to study their cycling stability. Li@Cu-Ni|Li@Cu-Ni symmetrical cells show stable voltage profiles with a small voltage hysteresis (about 26 mV) over 1500 hours at  $1 \text{ mA cm}^{-2}$  and  $1 \text{ mA h cm}^{-2}$ , whereas the voltage hystereses of Li@NF|Li@NF and Li@CF|Li@CF symmetrical cells increase gradually and show a tendency of extreme instability (Fig. 3d and e). There exhibits a similar stable long-cycle voltage profiles, when Li@Cu-Ni|Li@Cu-Ni symmetrical cells run at  $5 \text{ mA cm}^{-2}$  (Fig. S12, ESI†). Even if the current density increases to  $10 \text{ mA cm}^{-2}$ , Li@Cu-Ni|Li@Cu-Ni symmetrical cells still show more stable voltage profiles and longer cycling times at a high current density. In contrast, more severe voltage fluctuations and shorter cycling lives are obtained for Li@NF|Li@NF and Li@CF|Li@CF symmetrical cells (Fig. 3f and g). The uneven deposition of  $\text{Li}^+$  and the growth of Li dendrites on the lithiophobic CF and NF can result in different electrochemical

environment for the electrodes in symmetrical cells, which is the main reason for the asymmetry of the overpotential. At different current densities, the voltage hysteresis of Cu–Ni is less than those of CF and NF, indicating that the lithiophobicity/lithiophilicity transformation caused by the electron cloud migration effect has greatly improved the electrochemical performance (Fig. S13, ESI†). The different cycling current densities and cycling life of various reported 3D hosts and this work were compared and are presented in Fig. S14 and Table S2.† It can be clearly seen that Cu–Ni shows superior electrochemical performance under different test conditions. Other than that, the rate performance is presented in Fig. S15,† the voltage hysteresis of Li@Cu–Ni is smaller and more stable than those of other samples at any current density, indicating the excellent reversibility of Li@Cu–Ni anodes. In order to further explore the transport behaviour of  $\text{Li}^+$ , the activation energy ( $E_a$ ) calculated by fitting electrochemical impedance spectra (EIS) can clearly illustrate the difficulty level of the transference of  $\text{Li}^+$ . Obviously, compared to Li@NF and Li@CF, it was calculated that Li@Cu–Ni has a lower activation energy (58.594 kJ mol<sup>-1</sup>), which is beneficial for  $\text{Li}^+$  transportation (Fig. S16a–d and Fig. S17, ESI†).<sup>45,46</sup>

Density functional theory (DFT) calculations based on the first principles were employed to investigate the thermodynamic adsorption of Li. The adsorbed models of single Li on crystal surfaces including Cu, Ni, and Cu–Ni exposed to the (001) facet are studied (Fig. 4a–c), and the corresponding adsorption energies ( $E_{\text{ad}}$ ) were calculated to be  $-2.97$ ,  $-3.43$ , and  $-3.61$  eV, respectively. As a comparison, Cu–Ni is more toiless for Li deposition with the lowest adsorption energies, due to the electron cloud migration effect. The obtained electron density differences further demonstrate the results. As shown in Fig. 4d–f, the charge density around the Cu atom increases, while that around the Ni atom decreases, which is consistent with the XPS results. There is evident charge redistribution onto the surface of Cu–Ni due to the electron cloud migration effect. The charge density around the Cu and Ni atoms neutralize with each other, resulting in uniform electric field distribution inside Cu–Ni.<sup>47</sup> This can be beneficial for the uniform adsorption of the Li atom and restrict the formation of Li dendrites. Thus, the Li plating/stripping behaviour can be significantly improved by adjusting the electron cloud migration in Cu–Ni. The plating/stripping process of Li on Cu–Ni, NF and CF are shown in Fig. 4g and h, respectively. Lithium can deposit and dissolve uniformly on Cu–Ni, while NF and CF can aggravate the growth of lithium dendrites and produce “dead lithium” and cavities. The crystal models for Cu, Ni and Cu–Ni are shown in Fig. S18.†

To further investigate the Li deposition process, the amount of deposited Li was controlled from 1 to 3 mA h cm<sup>-2</sup> at a current density of 0.5 mA cm<sup>-2</sup>. As shown in Fig. 5a–c, we can see clearly that during the continuous deposition of Li, Cu–Ni shows a smooth surface without obvious lithium dendrites, thus guaranteeing excellent electrochemical perform-

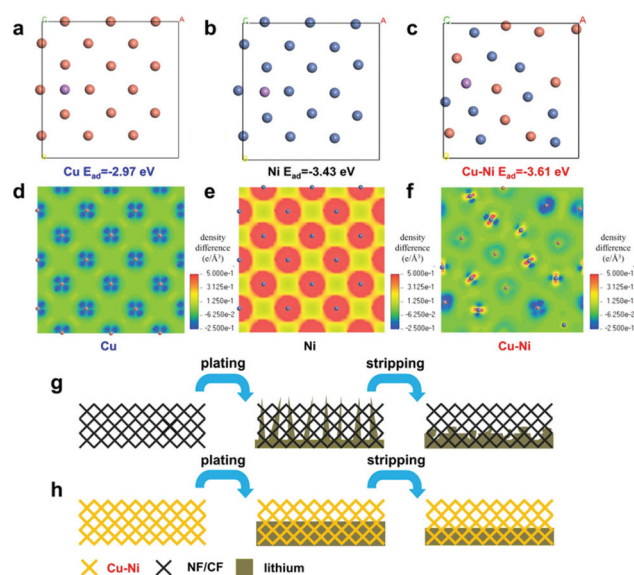


Fig. 4 Electron density difference calculations and the lithium deposition/dissolution mechanism. The crystal models with one Li atom adsorbed for (a) Cu, (b) Ni, and (c) Cu–Ni. The orange ball is the Cu atom. The blue ball is the Ni atom and the purple ball is the Li atom. Electron density difference of (d) Cu, (e) Ni, and (f) Cu–Ni. Schematic representation of the Li deposition/dissolution process on (g) NF/CF and (h) Cu–Ni.

ance. In contrast, at the initial stage of Li deposition, a small amount of lithium dendrites has appeared unevenly on the surface of NF and CF (Fig. 5d and g). Upon the increase of the deposition capacity, both the amount and diameter of lithium dendrites have increased dramatically, which will seriously reduce the CE and even pose a huge threat to battery safety (Fig. 5e, f, h, and i). In addition to the deposition behaviour of Li, the dissolution behaviour of Li is also very important. As a result, there appear a lot of cavities (red circle) and “dead lithium” (yellow circle) on the surface of CF and NF after 20 cycles (Fig. S19a and b, ESI†). The rough surface will aggravate the growth of lithium dendrites and the fracture of the SEI. With the help of lithiophilicity induced by the electron cloud migration effect, the surface of Cu–Ni is very smooth and there is no “dead lithium”, which will greatly improve the cycling stability and CE. The scattered particles on the surface are Cu–Ni bimetallic particles (Fig. S19c, ESI†).

In order to verify the practical performance of Li@Cu–Ni, Li@NF and Li@CF, these electrodes were designed as anodes in full cells with the LFP cathode. The assembled full cells are denoted respectively as Li@Cu–Ni||LFP, Li@NF||LFP, and Li@CF||LFP. The Li@Cu–Ni||LFP cells maintain a stable CE (96.67%) after 100 cycles, suggesting high reversibility. While the discharge capacity of the Li@NF||LFP cells is only 34.91 mA h g<sup>-1</sup> and the CE is 78.84% after 100 cycles. For the Li@CF||LFP cells, the cycling fluctuations are greater, and the capacity decays faster (Fig. 6a). The rapid failure of the cells is mainly caused by the uncontrolled growth of lithium den-

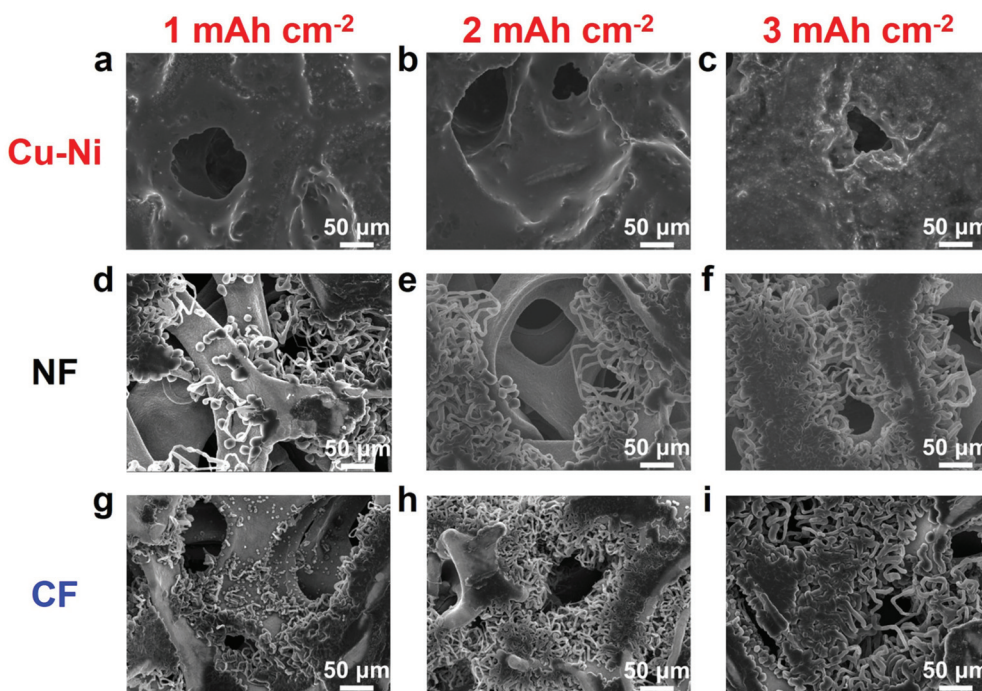


Fig. 5 Morphological characterization of different lithium deposition amounts. SEM images of (a–c) Cu–Ni, (d–f) CF and (g–i) NF with different lithium loadings: (a, d and g) 1 mA h cm<sup>-2</sup>, (b, e and h) 2 mA h cm<sup>-2</sup> and (c, f and i) 3 mA h cm<sup>-2</sup>.

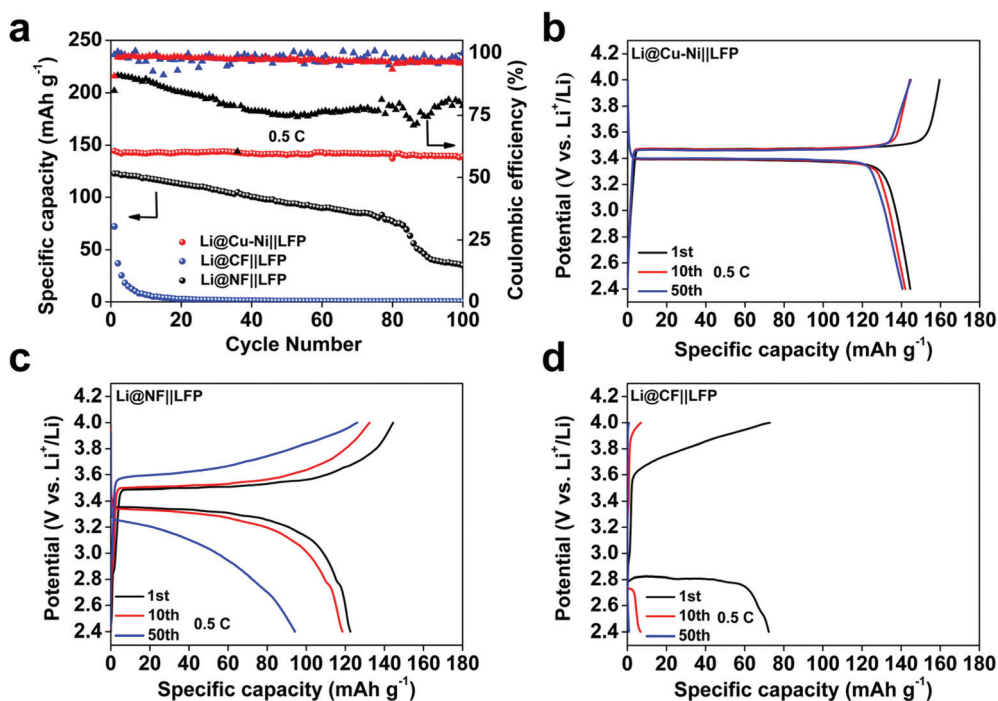


Fig. 6 Full cell performance of Li@Cu–Ni, Li@NF and Li@CF. (a) Cycling performance of Li@Cu–Ni||LFP, Li@NF||LFP and Li@CF||LFP cells at 0.5 C. Voltage profiles of the (b) Li@Cu–Ni||LFP cell, (c) Li@NF||LFP cell and (d) Li@CF||LFP cell.

drites. The galvanostatic charge–discharge voltage profiles at 0.5 C are shown in Fig. 6b–d, it can be clearly found that the overpotential of Li@Cu–Ni||LFP is smaller and more stable

than that of NF and CF from the 1<sup>st</sup> cycle to the 50<sup>th</sup> cycle. The improvement of the cycling stability and CE can indicate the superiority of dendrite-free Li@Cu–Ni composite anodes.

## Conclusions

In summary, our research results indicate that Cu–Ni exhibits excellent lithiophilicity, which can effectively regularize the deposition/dissolution process of Li and prevent the sprouting of lithium dendrites. The electron cloud migration effect caused by the different electronegativities of Cu and Ni can reshape the distribution of the surface charge density, leading to lithiophobicity/lithiophilicity transformation. According to the theoretical calculation results, it can be seen that there is a stronger adsorption energy between Li and Cu–Ni. The Li@Cu–Ni symmetrical cells show excellent stability and long cycling time (>1500 hours) at 1 mA cm<sup>-2</sup>. Furthermore, full cells assembled with LFP as the cathode still show a stable CE after 100 cycles. This strategy of modifying lithium metal anodes provides a new perspective of developing stable and safe lithium metal batteries for new generation energy storage systems.

## Conflicts of interest

There are no conflicts of interest to declare.

## Acknowledgements

This work was supported by the National Natural Science Foundation of China (51802239), the National Key Research and Development Program of China (2020YFA0715000), the Foshan Xianhu Laboratory of the Advanced Energy Science and Technology Guangdong Laboratory (XHT2020-005, XHT2020-003), the Natural Science Foundation of Hubei Province (2019CFA001), the National Key Research and Development Program of China (2019YFA0704902), the Fundamental Research Funds for the Central Universities (2020III011GX, 2020IVB057, 2019IVB054, and 2019III062JL), and National Innovation and Entrepreneurship Training Program for College Students (202010497005).

## Notes and references

- B. Dunn, H. Kamath and J. M. Tarascon, *Science*, 2011, **334**, 928–935.
- J. B. Goodenough and K. S. Park, *J. Am. Chem. Soc.*, 2013, **135**, 1167–1176.
- V. G. Pol and M. M. Thackeray, *Energy Environ. Sci.*, 2011, **4**, 1904–1912.
- J. F. Zhang, Y. P. Su and Y. G. Zhang, *Nanoscale*, 2020, **12**, 15528–15559.
- X. B. Cheng, R. Zhang, C. Z. Zhao and Q. Zhang, *Chem. Rev.*, 2017, **117**, 10403–10473.
- D. A. Dornbusch, R. Hilton, S. D. Lohman and G. J. Suppes, *J. Electrochem. Soc.*, 2015, **162**, A262–A268.
- L. Wang, Z. Y. Zhou, X. Yan, F. Hou, L. Wen, W. B. Luo, J. Liang and S. X. Dou, *Energy Storage Mater.*, 2018, **14**, 22–48.
- K. Yan, H. W. Lee, T. Gao, G. Y. Zheng, H. B. Yao, H. T. Wang, Z. D. Lu, Y. Zhou, Z. Liang, Z. F. Liu, S. Chu and Y. Cui, *Nano Lett.*, 2014, **14**, 6016–6022.
- K. Liu, A. Pei, H. R. Lee, B. Kong, N. Liu, D. C. Lin, Y. Y. Liu, C. Liu, P. C. Hsu, Z. N. Bao and Y. Cui, *J. Am. Chem. Soc.*, 2017, **139**, 4815–4820.
- K. Xu, *Chem. Rev.*, 2004, **104**, 4303–4417.
- F. Sun, R. Moroni, K. Dong, H. Markötter, D. Zhou, A. Hilger, L. Zielke, R. Zengerle, S. Thiele, J. Banhart and I. Manke, *ACS Energy Lett.*, 2016, **2**, 94–104.
- A. Aryanfar, D. J. Brooks, A. J. Colussi and M. R. Hoffmann, *Phys. Chem. Chem. Phys.*, 2014, **16**, 24965–24970.
- C. C. Fang, J. X. Li, M. H. Zhang, Y. H. Zhang, F. Yang, J. Z. Lee, M. H. Lee, J. Alvarado, M. A. Schroeder, Y. Y. C. Yang, B. Y. Lu, N. Williams, M. Ceja, L. Yang, M. Cai, J. Gu, K. Xu, X. F. Wang and Y. S. Meng, *Nature*, 2019, **572**, 511–515.
- R. Tao, X. X. Bi, S. Li, Y. Yao, F. Wu, Q. Wang, C. Z. Zhang and J. Lu, *ACS Appl. Mater. Interfaces*, 2017, **9**, 7003–7008.
- X. Chen, T. Z. Hou, B. Li, C. Yan, L. Zhu, C. Guan, X. B. Cheng, H. J. Peng, J. Q. Huang and Q. Zhang, *Energy Storage Mater.*, 2017, **8**, 194–201.
- Y. Nan, S. M. Li, B. Li and S. B. Yang, *Nanoscale*, 2019, **11**, 2194–2201.
- Y. X. Yuan, F. Wu, Y. R. Liu, X. R. Wang, K. Zhang, L. M. Zheng, Z. H. Wang, Y. Bai and C. Wu, *ACS Appl. Mater. Interfaces*, 2020, **12**, 39362–39371.
- H. M. Zhang, X. B. Liao, Y. P. Guan, Y. Xiang, M. Li, W. F. Zhang, X. Zhu, H. Ming, L. Lu, J. Qiu, Y. Huang, G. Cao, Y. Yang, L. Q. Mai, Y. Zhao and H. Zhang, *Nat. Commun.*, 2018, **9**, 3729.
- N. W. Li, Y. X. Yin, C. P. Yang and Y. G. Guo, *Adv. Mater.*, 2016, **28**, 1853–1858.
- Q. C. Liu, J. J. Xu, S. Yuan, Z. W. Chang, D. Xu, Y. B. Yin, L. Li, H. X. Zhong, Y. S. Jiang, J. M. Yan and X. B. Zhang, *Adv. Mater.*, 2015, **27**, 5241–5247.
- J. G. Wan, J. Xie, D. G. Mackanic, W. Burke, Z. N. Bao and Y. Cui, *Mater. Today Nano*, 2018, **4**, 1–16.
- A. Manthiram, X. W. Yu and S. F. Wang, *Nat. Rev. Mater.*, 2017, **2**, 16103.
- Y. Kato, S. Hori, T. Saito, K. Suzuki, M. Hirayama, A. Mitsui, M. Yonemura, H. Iba and R. Kanno, *Nat. Energy*, 2016, **1**, 16030.
- G. M. Stone, S. A. Mullin, A. A. Teran, D. T. Hallinan, A. M. Minor, A. Hexemer and N. P. Balsara, *J. Electrochem. Soc.*, 2012, **159**, A222–A227.
- X. B. Chen and P. M. Vereecken, *Adv. Mater. Interfaces*, 2018, **6**, 1800899.
- D. C. Lin, Y. Y. Liu and Y. Cui, *Nat. Nanotechnol.*, 2017, **12**, 194–206.
- R. Xu, X. B. Cheng, C. Yan, X. Q. Zhang, Y. Xiao, C. Z. Zhao, J. Q. Huang and Q. Zhang, *Matter*, 2019, **1**, 317–344.
- Z. Zhu, R. Y. Kan, S. Hu, L. He, X. F. Hong, H. Tang and W. Luo, *Small*, 2020, **16**(39), 2003251.
- K. Li, Z. Y. Hu, J. Z. Ma, S. Chen, D. X. Mu and J. T. Zhang, *Adv. Mater.*, 2019, **31**, 1902399.

- 30 C. Zhang, R. Y. Lyu, W. Lv, H. Li, W. Jiang, J. Li, S. C. Gu, G. M. Zhou, Z. J. Huang, Y. B. Zhang, J. Q. Wu, Q. H. Yang and F. Y. Kang, *Adv. Mater.*, 2019, **31**, 1904991.
- 31 Z. H. Li, X. L. Li, L. Zhou, Z. C. Xiao, S. K. Zhou, L. D. Li and L. J. Zhi, *Nanoscale*, 2018, **10**, 4675–4679.
- 32 Y. X. Yuan, F. Wu, Y. Bai, Y. Li, G. H. Chen, Z. H. Wang and C. Wu, *Energy Storage Mater.*, 2019, **16**, 411–418.
- 33 J. K. Chang, S. H. Hsu, I. W. Sun and W. T. Tsai, *J. Phys. Chem. C*, 2008, **112**, 1371–1376.
- 34 K. Yan, Z. D. Lu, H. W. Lee, F. Xiong, P. C. Hsu, Y. Z. Li, J. Zhao, S. Chu and Y. Cui, *Nat. Energy*, 2016, **1**, 16010.
- 35 J. J. Teo, Y. Chang and H. C. Zeng, *Langmuir*, 2006, **22**, 7369–7377.
- 36 A. Quintana, E. Menendez, E. Isarain-Chavez, J. Fornell, P. Solsona, F. Fauth, M. D. Baro, J. Nogues, E. Pellicer and J. Sort, *Small*, 2018, **14**, 1704396.
- 37 W. B. Wang, Y. B. Zhu, Q. L. Wen, Y. T. Wang, J. Xia, C. C. Li, M. W. Chen, Y. W. Liu, H. Q. Li, H. A. Wu and T. Y. Zhai, *Adv. Mater.*, 2019, **31**, 1900528.
- 38 M. X. Li, H. Y. Wang, W. D. Zhu, W. M. Li, C. Wang and X. F. Lu, *Adv. Sci.*, 2020, **7**, 1901833.
- 39 M. A. Ahsan, A. R. P. Santiago, Y. Hong, N. Zhang, M. Cano, E. Rodriguez-Castellon, L. Echegoyen, S. T. Sreenivasan and J. C. Noveron, *J. Am. Chem. Soc.*, 2020, **142**, 14688–14701.
- 40 M. H. Luo, W. P. Sun, B. B. Xu, H. G. Pan and Y. Z. Jiang, *Adv. Energy Mater.*, 2021, **11**, 2002762.
- 41 C. H. Zhao, Y. F. Li, W. Q. Zhang, Y. Zheng, X. M. Lou, B. Yu, J. Chen, Y. Chen, M. L. Liu and J. C. Wang, *Energy Environ. Sci.*, 2020, **13**, 53–85.
- 42 L. An, Z. Y. Zhang, J. R. Feng, F. Lv, Y. X. Li, R. Wang, M. Lu, R. B. Gupta, P. X. Xi and S. Zhang, *J. Am. Chem. Soc.*, 2018, **140**, 17624–17631.
- 43 H. Ye, Z. J. Zheng, H. R. Yao, S. C. Liu, T. T. Zuo, X. W. Wu, Y. X. Yin, N. W. Li, J. J. Gu, F. F. Cao and Y. G. Guo, *Angew. Chem., Int. Ed.*, 2019, **58**, 1094–1099.
- 44 C. K. Chan, H. L. Peng, G. Liu, K. McIlwrath, X. F. Zhang, R. A. Huggins and Y. Cui, *Nat. Nanotechnol.*, 2008, **3**, 31–35.
- 45 C. Yan, H. R. Li, X. Chen, X. Q. Zhang, X. B. Cheng, R. Xu, J. Q. Huang and Q. Zhang, *J. Am. Chem. Soc.*, 2019, **141**, 9422–9429.
- 46 X. S. Xie, S. Q. Liang, J. W. Gao, S. Guo, J. B. Guo, C. Wang, G. Y. Xu, X. W. Wu, G. Chen and J. Zhou, *Energy Environ. Sci.*, 2020, **13**, 503–510.
- 47 R. Li, J. X. Wang, L. D. Lin, H. Wang, C. M. Wang, C. H. Zhang, C. H. Song, F. Tian, J. Yang and Y. T. Qian, *Mater. Today Energy*, 2020, **15**, 100367.